Supporting Information

Solvent and Wavelength-Dependent Photoluminescence Relaxation Dynamics of Carbon Nanotube *sp*^{3} Defect States

Xiaowei He[1,#], Kirill A. Velizhanin[2,#], George Bullard[3], Yusong Bai[3], Jean-Hubert Olivier[3†], Nicolai F. Hartmann[1], Brendan J. Gifford[2,4,5], Svetlana Kilina[5], Sergei Tretiak[1,2], Han Htoon[1], Michael J. Therien[3], Stephen K. Doorn[1]*

[1]Center for Integrated Nanotechnologies, Materials Physics and Applications Division, Los Alamos National Laboratory, Los Alamos, NM 87545

[2]Theoretical Division, Los Alamos National Laboratory, Los Alamos, NM 87545

[3]Department of Chemistry, French Family Science Center, Duke University, Durham, NC 27708

[4]Center for Nonlinear Sciences, Los Alamos National Laboratory, Los Alamos, NM 87545

[5]Department of Chemistry and Biochemistry, North Dakota State University, Fargo, ND 58108

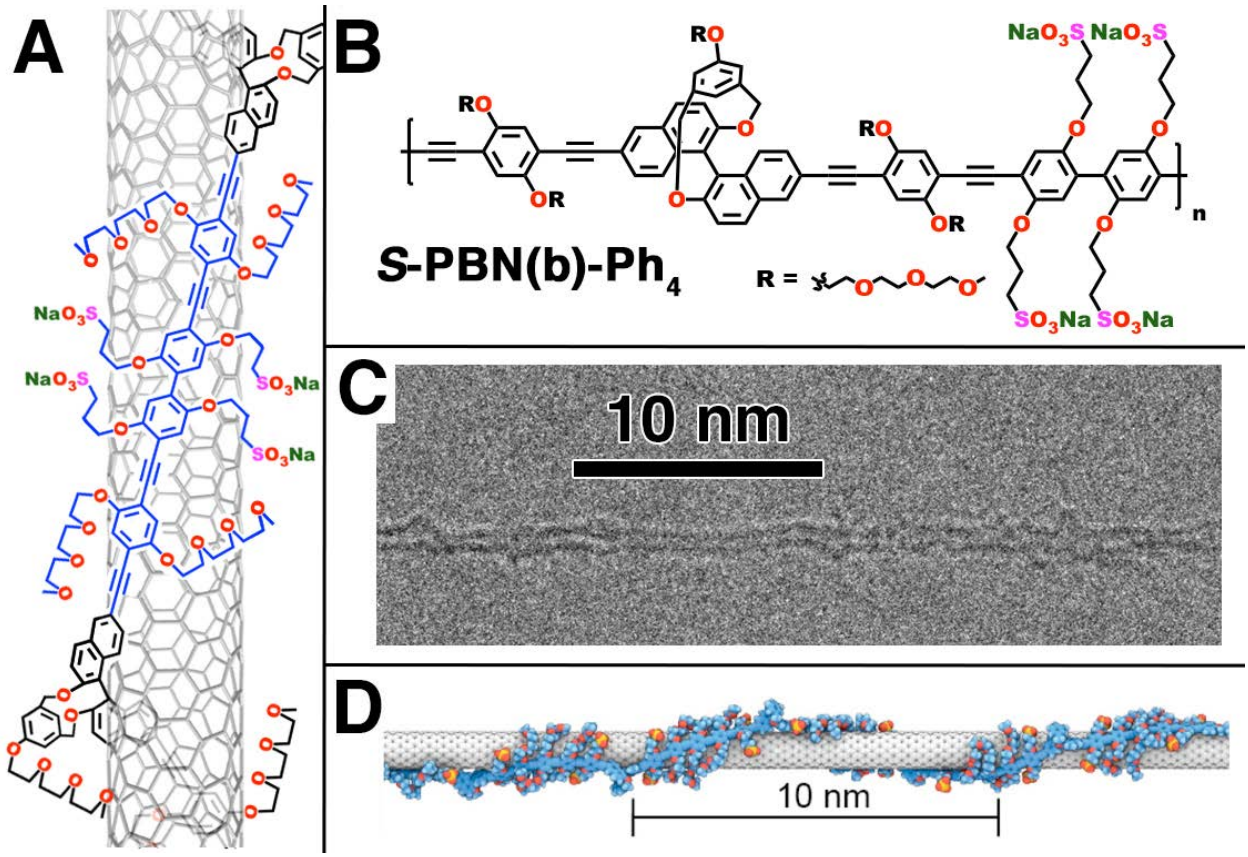

Figure S1. Morphological characteristics of polymer-SWCNT superstructure composites. (a) Schematic illustrating single-handed helical wrapping of a SWCNT surface with arylene-ethynylene polymer. (b) Depiction of chiral semiconducting S-PBN(b)-Ph_4 polymer used in these studies. (c) TEM image highlighting single-chain nanotube wrapping at a fixed helical pitch length. (d) A MD simulation of a chiral polymer wrapping of the SWNT surface.

	Dielectric constant	E11 (nm)	E11*(nm)	E11*-(nm)
H2O	80	1013	1162	1283
D2O	80	1011	1164	1284
DMF	36.7	1011	1162	1284
MeOH	32.7	1011	1167	1284
THF	7.58	1008	1153	1285
Toluene+THF	3	1008	1157	1284

Table S1. Solvent dielectric constant and peak PL emission wavelengths for band-edge exciton (E_{11}) and defect states (E_{11}* and E_{11}*$^-$) for 4-methoxybenzene-functionalized (6,5) SWCNTs wrapped with S-PBn(b)-Ph4 polymer.

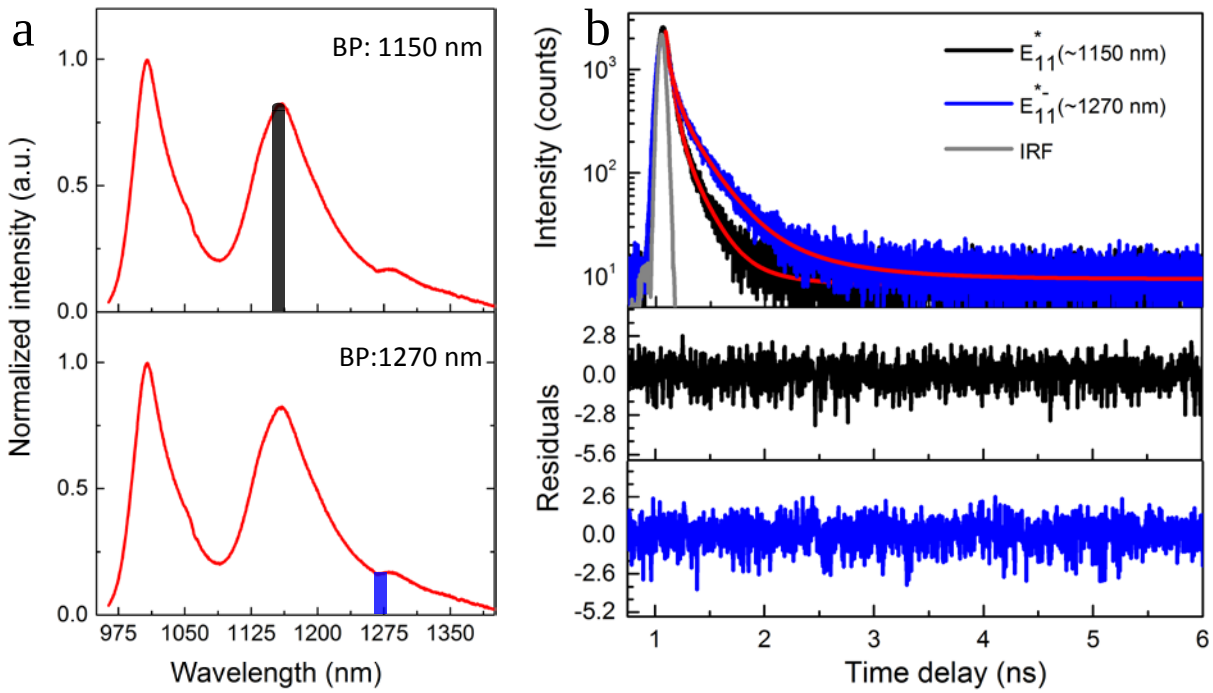

Figure S2. Reconvolution fitting of defect-state PL deay. Examples given for 4-methoxybenzene-functionalized (6,5) SWCNTs suspended in H_2O for the two emission bands highlighted in a) centered at 1150 nm (E_{11}*, black) and 1270 nm (E_{11}*$^-$, blue). b) PL decay traces for E_{11}* (black) and E_{11}*$^-$ (blue). Fits to decays (red) using a biexponential reconvolution model are overlaid, with instrument response function (IRF) shown in gray. Residuals for the two fits are shown below.

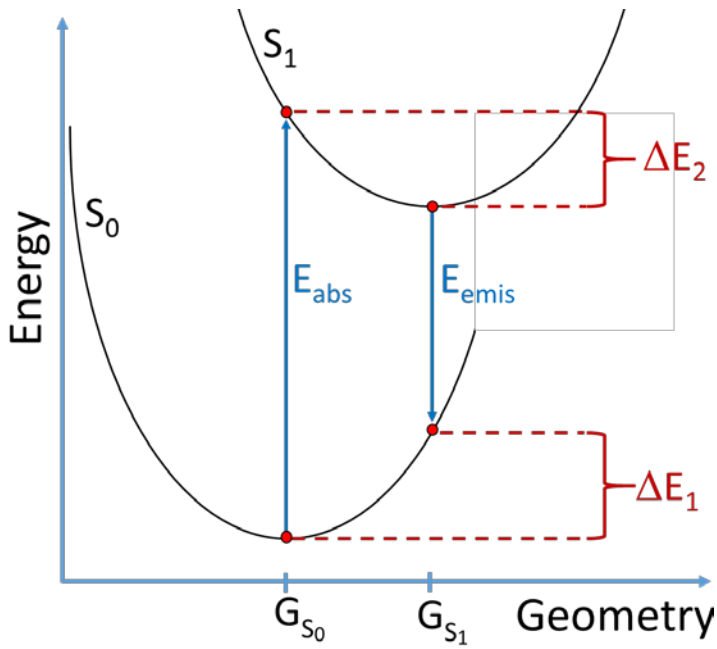

Figure S3. Schematic of the potential energy surface and computational parameters from which reorganization energies associated with defect-state excitation (ΔE_2) and emission (ΔE_1) were calculated.

Configuration		E_{abs} (eV)	E_{emis} (eV)	Absorption Transition Dipole	Emission Transition Dipole	Radiative Lifetime (ns)	ΔE_1 (eV)	ΔE_2 (eV)
Ortho	L_{30}	1.6082	1.4025	36.2	36.2	1.68	0.101	0.104
	L_{90}	1.8384	1.6536	40.1	38.7	0.90	0.095	0.089

Table S2. TDDFT results for 4-mexthoxybenzene-functionalized (6,5) SWCNTs, including energies of absorption and emission, transition dipoles, radiative lifetimes, and reorganization energies calculated from excited state parameters for the experimentally relevant species. Aryl functionalization of SWCNTs generates different binding configurations on the SWCNT surface, designated by their orientation with respect to the SWCNT axis.[1] The ortho-L_{30} configuration is attributed to the E_{11}^{*-} emission features, while the ortho-L_{90} configuration is attributed to E_{11}^{*}. See ref. 1 for a complete description of possible binding configurations.

I. Dependence of Radiative Relaxation Rate on Electronic State, Corresponding Oscillator Strength, and Solvent Dielectric Constant.

The magnitude of the transition dipole moment of the trapped exciton negatively correlates with the trapping energy, that is the stronger is the trapping the weaker is the transition dipole moment. This phenomenon, readily observed in DFT calculations (see Table S2) is rationalized as follows. The exciton wavefunction can be represented as $\Psi_x = \phi_x(R)\varphi(r_{eh})$, where $\phi_x(R)$ with $R = (r_e + r_h)/2$ encodes the center-of-mass motion of the bound electron-hole pair, and $\varphi(r_{eh})$ encodes the relative motion of the electron and the hole within the center-of-mass frame ($r_{eh} = r_e - r_h$). A photon carries essentially zero momentum and therefore can only couple to excitonic transitions via the zero-momentum Fourier component of the exciton envelope wavefunction $\phi_x(R)$.[2-4] We refer to the spatial extent of $\phi_x(R)$ in a SWCNT as the exciton localization radius, R_x. Within the effective mass approximation for the exciton, the trapping energy should be proportional to $1/R_x^2$. The amplitude of the zero-momentum Fourier component of $\phi_x(R)$ is proportional to $\int \phi_x(R)dR \sim \sqrt{R_x}$. Therefore, an exciton sitting in a deeper trap (and so emitting at longer wavelengths) is more weakly coupled to photons, which increases its radiative lifetime.

The rate of radiative recombination is given by $k_r \propto (\hbar\omega)^3|d|^2$,[5] where $\hbar\omega$ is the transition energy and d is the transition dipole. Therefore, even if the magnitude of the transition dipole does not depend on the exciton trapping energy, the radiative lifetime would still increase when the PL energy decreases. These two factors both result in higher PL lifetimes at longer emission wavelength, which qualitatively agrees with the trends seen in Figure 3 of the main text. However, DFT calculations suggest that the magnitude of the PL lifetime for the systems of interest is expected to be on the order of nanoseconds (Table S2) and the observed PL lifetimes in Figure 3 are at least a factor of 10 smaller. The radiative recombination channel thus contributes negligibly to the observed exciton relaxation lifetimes and the wavelength dependence of the radiative lifetime cannot be the source of the observed wavelength dependence in Figure 3.

To finish the discussion on the radiative lifetime, we briefly consider the effect of the dielectric screening on the exciton-photon coupling. This effect comes from three different factors: (i) the radiative recombination rate increases with the dielectric permittivity of the solvent, ϵ, because the photon density of state increases with ϵ,[6] (ii) the difference in effective dielectric permittivities of SWCNT and solvent can result in dielectric screening of the photon electric field,[7] and (iii) screening of the electron-hole Coulomb interaction results in the average electron-hole distance becoming a function of the dielectric permittivity of solvent, which in turn affects the exciton oscillator strength.[8] In practice, however, the effect of dielectric permittivity on the radiative recombination rate is rather weak when all three factors are considered. Specifically, it is $k_r \propto \sqrt{\epsilon}$ for the first factor.[6] The second factor actually does not affect k_r for excitons polarized along the SWCNT axis (the case for all states considered here) because the excitonic transitions corresponding to these excitons only couple to photons through the electric field parallel to the tube axis. The magnitude of such electric field is not affected by the SWCNT-solvent interface because they are parallel.[7] As for the third factor, the radiative recombination rate is approximately inversely proportional to the mean electron-hole separation

distance L_{eh}, which in turn is linearly proportional to the dielectric permittivity of the solvent.[8] The key observation is that for each of these factors the dielectric permittivity must be evaluated at optical frequencies. This is rather obvious for the first two factors,[6,9] and can be shown to be true for excitons in materials where electrons and holes have similar effective masses,[10] as is the case for SWCNTs. Collecting all the three factors together, $k_r \propto \sqrt{\epsilon} \times 1 \times \frac{1}{\epsilon} = \frac{1}{\sqrt{\epsilon}}$, and accounting for the fact that for all the considered solvents the dielectric permittivity at optical wavelengths is bound to a narrow range between 1.7 and 2.2, one obtains at most ~20% variations in the radiative lifetimes in different solvents. This weak variation cannot of course affect the conclusion made above that the radiative recombination channel contributes negligibly to the observed PL lifetimes.

II. Electronic-to-Vibrational Energy Transfer (EVET).

In this section we discuss the efficiency of the electronic-to-vibrational energy transfer (EVET) from a SWCNT to the surrounding solvent. The accurate evaluation of an EVET rate in such a system is a very complex task since the emitter (SWCNT) is *extended*, that is the characteristic (average) distance between emitter's atoms and the solvent can be significantly smaller than the exciton localization length. In what follows, we will not attempt to evaluate the EVET rate accurately, but rather introduce the general framework and then obtain an approximate expression for the rate using plausible semi-quantitative arguments.

General expression for EVET rate. According to Bohr's correspondence principle between quantum and classical mechanics, a two-state quantum emitter can be thought of as a classical oscillating dipole. Such a dipole generates an electric field around itself (we do not consider retardation effects here and work in the near-field zone) that polarizes the medium (e.g., solvent). This polarization induces an electric field, which in turn acts on the original dipole. Specifically, the dot product of the *induced* electric field on the instantaneous electric current of the oscillating dipole moment is the time derivative of the energy of the oscillating dipole. Typically, this time derivative is negative (when averaged over the period of oscillations) meaning that the oscillating dipole loses energy to the medium via this "self-interaction". The following general expression gives the relaxation rate of the emitter due to these energy losses (derivation is omitted)

$$\Gamma = -\frac{2}{\hbar}\int dx^3 dx'^3\, \rho_{10}(x) V''(x,x';\omega)\rho_{10}(x'), \tag{1}$$

where $\rho_{10}(x)$ is the amplitude of the oscillating charge density of the emitter. From the more rigorous quantum mechanical perspective, this is a spatially distributed transition charge density

$$\rho_{10}(x) = \langle 1|\hat{\rho}(x)|0\rangle, \tag{2}$$

where $\hat{\rho}(x)$ is the operator of charge density; $|0\rangle$ and $|1\rangle$ are, respectively, the ground and electronic excited states of the two-state emitter. The Green's function of the Poisson problem (the exact total electric field potential at position x induced by a unit charge located at position x') is denoted by $V(x,x';\omega)$, and V'' stands for its imaginary part. Angular frequency of the

oscillating dipole is ω, and correspondingly $E_{10} = \hbar\omega$ is the energy gap between the ground and excited states of the quantum emitter. The Green's function of the Poisson problem depends on this frequency since dielectric functions are ω-dependent. In particular, the imaginary part of the Green's function is only non-vanishing if the imaginary part of the dielectric function at this frequency is not zero. As is seen, Eq. (1) represents a self-interaction, where the transition density of the emitter interacts with itself via the induced electric field potential. Eq. (1) can be accurately derived considering how a "bare" quantum-mechanical (many-body) Green's function of the two-state emitter is being "dressed" by the interaction with the environment. Such "dressing" can be represented by a self-energy term that shifts the "bare" energy of the emitter. Accordingly, the real part of the self-energy is a simple real energy shift, which is small and is typically neglected. The imaginary part of the self-energy, which is interpreted as the decay rate, is Eq. (1).

If the quantum emitter can be approximated as a pointwise dipole, then Eq. (1) reduces to the following well-known expression[9]

$$\Gamma_{pd} = \frac{2}{\hbar} d_{10} G'' d_{10}, \tag{3}$$

where d_{10} is the transition dipole moment of the emitter, and G is the electric field produced by a pointwise dipole at the position of this dipole. Eq. (1) describes the rate of energy transfer from the electronic excited state of the emitter to arbitrary excitations of the medium, as long as these latter excitations are captured by the frequency-dependent complex dielectric function of the medium. In this paper, we are interested in the energy transfer to combination vibrational bends, which render certain polar solvents (e.g., water)[11] absorptive (i.e., imaginary part of the dielectric function does not vanish) at optical wavelengths of 1000-1300 nm (~0.95-1.2 eV).

EVET for "large" semiconductor nano-sized systems. Single-particle wavefunctions for semiconductor nano-sized systems (e.g., semiconductor quantum dot, SWCNT) can often be accurately represented, within the so-called envelope function approximation, as a product of the slowly varying envelope function and the rapidly oscillating bulk part. The former part encodes quantum confinement. The latter part comes from the bulk Bloch function, which is periodic over a bulk unit cell and knows nothing about quantum confinement. This approximation is accurate as long as the exciton localization size is much larger than the bulk lattice constant. For example, in colloidal semiconductor quantum dots (QD) the exciton localization size is typically the same as the QD size, which could be several nanometers. Under these conditions, the envelope function approximation applies.[12] In covalently functionalized semiconductor SWCNTs, the localization size of the trapped exciton can be on the order of several nanometers (see Figure S5 in Supporting Information for Ref. 1) which is significantly larger than the carbon-carbon distance (the effective lattice constant in this material), so the envelope function approximation again applies.

We assume that our nano-sized systems are "large" in the sense that they are made up of a large number of bulk unit cells, so that the envelope function approximation is accurate. Under this approximation, the transition charge density can be thought of as being composed by a large number of small dipoles, where each dipole represents a particular bulk unit cell within a nano-sized system. If the "size" of each such small dipole (i.e., the size of the bulk unit cell) is smaller

than the characteristic distance between these dipoles and the medium, the transition charge density $\rho_{10}(x)$ can be related to the continuous smoothly varying dipole density $P_{10}(x)$ as $\rho_{10}(x) = -\nabla_x P_{10}(x)$. The EVET rate is then given by

$$\Gamma = -\frac{2}{\hbar}\int dx^3 dx'^3\, P_{10}(x)\frac{\partial}{\partial x}\frac{\partial}{\partial x'}V''(x,x';\omega)P_{10}(x'). \tag{4}$$

Additionally, if the characteristic distance between the dipoles and the medium is larger, or at least comparable to the size of the exciton localization, substituting the entire $P_{10}(x)$ with its pointwise dipole approximation $P_{10}(x) \to \delta(x)d_{10}$, where $d_{10} = \int dx\, P_{10}(x)$, should be a reasonable approximation. This approximation leads to Eq. (3). For a spherical semiconductor quantum dot (QD), both assumptions above are applicable, so the point dipole approximation, Eq. (3), can be expected to produce a reasonable approximate to the EVET rate. Solving the Poisson problem in the spherical geometry yields (derivation is not shown here)

$$\Gamma_{pd} = \hbar^{-1}\frac{|d_{10}|^2}{R^3}\frac{12\epsilon_s''}{(\epsilon_{QD}+2\epsilon_s')^2}, \tag{5}$$

where R and d_{10} are the radius and transition dipole moment of the QD, respectively. Solvent dielectric function is $\epsilon_s(\omega) = \epsilon_s'(\omega) + i\epsilon_s''(\omega)$, where, as above, ω corresponds to the transition energy. The QD dielectric function ϵ_{QD} is assumed real. Eq. (5) is exactly what was obtained in Ref. 11 for a spherical semiconductor QD.

The assumption above that the characteristic distance between the small dipole and the solvent medium is larger (or at least comparable to) the exciton localization size, allowed us to get from Eq. (4) to Eq. (5). This assumption is reasonable for spherical QDs, but is not valid for SWCNTs in a solvent. Indeed, the size of the bulk unit cell is on the order of the C-C distance (~1.4Å) and the distance between the SWCNT surface and the solvent (water) is ~3 Å.[13,14] Therefore, the slowly varying transition dipole density should still be a reasonable approximation. However, the effective size of the system (the localization size of the trapped exciton sitting near an sp^3 defect of the functionalized SWCNT) can be on the order of several nanometers (see Figure S5 in Supporting Information for Ref. 1), which is significantly larger than the small dipole-to-solvent distance. Under these conditions, the system becomes *extended*: the transition density of the trapped exciton cannot be represented as a point dipole and the full Eq. (4) or Eq. (1) must be used instead of Eq. (3). Comparing surface-to-solvent distance of ~3 Å to the exciton localization size of ~3-5 nm,[1] one has an aspect ratio, or degree of *extendedness*, of ~10. In the section to follow we consider the simplest possible 1D-extended model of EVET, where the effect of the extendedness can be observed and quantified. In particular, we will see that the effect of this 1D extendedness can be approximately captured within that simplest model by introducing an extra scaling prefactor into Eq. (3). We then add that prefactor to Eq. (5) to evaluate the EVET rate in the case of the functionalized SWCNT.

1D system near flat interface. Eq. (3) depends quadratically on the magnitude of the transition dipole. This means that if we split a single point dipole into two of equal magnitude and separate them sufficiently so that they do not interact, the effective EVET rate becomes two times smaller. We, therefore, expect that "spreading" a dipole by going from a point dipole to an extended system diminishes the EVET rate. To quantify this effect, we consider a simple model

of a 1D emitter sitting in vacuum parallel to a flat dielectric interface. The distance between the emitter and the surface of the dielectric (of dielectric constant ϵ) is denoted by h. The transition dipole density of the emitter is given by $P_{10}(x) = L^{-1}f(x/L)$ polarized along $the\ x$-direction, where $f(x)$ is a smooth normalized ($\int dx\, f(x) = 1$) function, which is maximized at $x \sim 0$ and decays quickly when $|x| \gtrsim 1$. Because of the normalization condition the overall transition dipole is of unit magnitude.

The electrostatic problem in this case is analytically solvable by the method of image charges yielding the Green's function of the Poisson equation along the 1D emitter as

$$V(x,x') = \frac{1}{|x-x'|} - \frac{\epsilon-1}{\epsilon+1}\frac{1}{\sqrt{4h^2+(x-x')^2}}, \tag{6}$$

where the first r.h.s. term is the direct through-vacuum interaction and the second r.h.s. term is the induced electrostatic potential. This latter term has a non-vanishing imaginary part, so the non-trivial part of the evaluation of the EVET rate for this model reduces to evaluation of the following integral

$$I = \int_{-\infty}^{\infty} dx \int_{-\infty}^{\infty} dx'\ \frac{\partial_x P_{10}(x)\partial_{x'} P_{10}(x')}{\sqrt{4h^2+(x-x')^2}}. \tag{7}$$

The Fourier transform of the kernel is $\int_{-\infty}^{\infty} dx\ \frac{e^{-ikx}}{\sqrt{4h^2+x^2}} = 2K_0(2|k|h)$, where K_0 is the modified spherical Bessel function of the second kind. Using this identity, the integral above transforms into

$$I = \frac{2}{\pi L^3}\int_0^{\infty} dk\ K_0(2kh/L)k^2|f(k)|^2, \tag{8}$$

where $f(k)$ is the Fourier transform of $f(x)$ introduced above. As is seen, the integral essentially depends on the ratio h/L, so we consider two limiting cases. If L is small ($h/L \gg 1$), K_0 decays very rapidly and the integral becomes

$$I \approx \frac{2|f(k=0)|^2}{\pi L^3}\int_0^{\infty} dk\ K_0\left(\frac{2kh}{L}\right)k^2 = \frac{f(k=0)}{8h^3} = \frac{1}{8h^3}. \tag{9}$$

This result assumes the Coulomb interaction potential of two parallel point dipoles that are perpendicular to the vector of length $2h$ that connects them. Physically it corresponds to the limiting case of the point dipole losing its energy via EVET thru interaction with its own image dipole.

When L is large ($h/L \ll 1$), we approximate the modified Bessel function as $K_0\left(\frac{2kh}{L}\right) \approx \ln\left(\frac{kh}{L}\right) - \gamma$, where $\gamma \approx 0.577$ is the Euler-Mascheroni constant. This is a slowly varying function and $kf(k)$ peaks at $k \sim 1$, giving

$$I \approx \frac{2}{\pi L^3}\left[\ln\left(\frac{h}{L}\right) - \gamma\right]\int_0^{\infty} dk\ k^2|f(k)|^2 \sim \frac{1}{L^3}\left[\ln\left(\frac{h}{L}\right) - \gamma\right]. \tag{10}$$

Here the similarity sign "~" means that the expression is known up to a numerical prefactor of the order 1. Figure S4 compares the results of the exact numerical evaluation of Eq. (8), using various approximations, where the dipole density distribution function is taken as $f(x) = \pi^{-1/2} e^{-x^2}$.

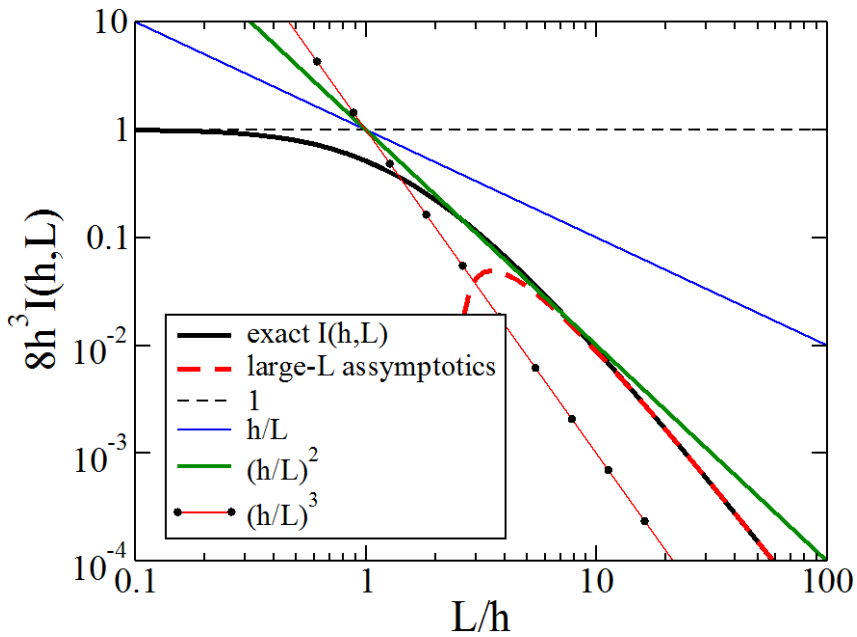

Figure S4. Exact numerical result for Eq. (8) is shown by thick black line. Dashed red line is Eq. (11).

The numerical result is shown by the thick black line. The integral is normalized by multiplying it by $8h^3$ so that it converges to 1 (thin dashed black line) when L is small, Eq. (9). Accurate large-L asymptotics, shown by thick dashed red line, can be obtained from Eq. (10) by evaluating the integral in the right-hand side exactly (since $f(x)$ is now specified), which yields

$$I = \sqrt{\frac{2}{\pi}} \frac{1}{L^3} \left[\ln\left(\frac{L}{\sqrt{2}h}\right) - \gamma \right]. \tag{11}$$

Finally, we attempt to approximate the numerical result by scaling the pointwise dipole result, Eq. (9), with a certain power of h/L, i.e., we have $I \approx \frac{1}{8h^3}\left(\frac{h}{L}\right)^{\alpha}$. Results for $\alpha = 1,2,3$ are shown by thin solid blue, magenta and red lines, respectively (Figure S4). Of these, $\alpha = 2$ agrees best with the numerical results at $L/h \sim 10$, which is exactly the aspect ratio of the "extended" dipole we are interested in (see above). This means that for the "extendedness" of ~ 10 the approximate expression for the EVET rate for the considered simple 1D model can be obtained by first evaluating the rate as if the dipole is pointwise, and then scaling the rate down by multiplying it with $(h/L)^2$ to account for the extendedness.

It is clear that if the localization length of a trapped exciton in a functionalized SWCNT were very small, then one would be able to use Eq. (5) directly. This is not the case. We modify Eq.

(5) by multiplying it by the same scaling factor of $(h/L)^2$, which was found to work well in the case of the simple 1D model. Therefore, we assume that the EVET rate for the trapped exciton in SWCNT is given by

$$\Gamma = \left(\frac{R_s}{R_x}\right)^2 \Gamma_{pd}, \tag{12}$$

where R_x is the localization "radius" of the exciton, and R_s is the solvation radius (distance from the SWCNT surface to the first solvation shell). As an expression for Γ_{pd} we take Eq. (5). Dielectric screening by a 1D system (i.e., SWCNT) is non-local in a sense that the effective dielectric function of screening in the proximity of the 1D object is distance-dependent and converges to the dielectric function of the medium at distances larger than the effective diameter of the 1D system. Since the characteristic exciton size is typically significantly larger than the SWCNT diameter, even for a trapped exciton, the effective dielectric constant can be considered to be that of the medium. Under these conditions, one has uniform dielectric screening and the expression for the EVET rate of the trapped exciton in SWCNT becomes

$$\Gamma_{pd} = \frac{|d_{10}|^2}{R_s^3} \frac{4\epsilon_s''}{3\epsilon_s'^2}, \tag{13}$$

III. Derivation of Expression for Long Lifetime Component Amplitude.

To rationalize the observed dependence of the long lifetime component amplitude on wavelength and the solvent, shown in Figure 6 in the main text, we solve for the dynamics of the relaxation of trapped exciton within a simple two-state model. The lowest state of the two-level system is assumed to be the bright trapped excitonic state, as found in Ref. [3] and also in this work (see Table S3 and Figure S5 below). We denote the rate constant of the exciton recombination from this bright state by k. Exciton from the higher-laying dark trapped state relaxes to the bright state with rate constant k_0. The reverse process of up-conversion from the bright to dark trapped state has the rate constant of $k_0' = k_0 e^{-\epsilon/kT}$, where ϵ is the energy separation between the two states. The direct exciton recombination from the dark state is assumed absent for the time being. The corresponding equations for the time evolution of populations of the two states are:

$$\frac{dp_d}{dt} = -k_0 p_d + k_0' p_b, \tag{14a}$$

$$\frac{dp_b}{dt} = k_0 p_d - (k + k_0') p_b. \tag{14b}$$

This system of linear ordinary differential equations can be solved exactly, and the general solution is a biexponential decay of the form

$$\begin{pmatrix} p_b(t) \\ p_d(t) \end{pmatrix} = \begin{pmatrix} A_s \\ B_s \end{pmatrix} e^{-t/\tau_s} + \begin{pmatrix} A_l \\ B_l \end{pmatrix} e^{-t/\tau_l}, \tag{15}$$

where the short and long decay times, τ_s and τ_l, respectively, are given by combinations of rate constants in Eq. (14). Amplitudes A_s, A_l, B_s, B_l are combinations of the rate constants and the initial populations of the dark and bright states, p_d^0 and $1 - p_d^0$, respectively. Eq. (15), with all the amplitudes and decay times expressed via initial populations and rate constants, becomes rather long and complicated. Instead, we provide here physically transparent solutions for the two limiting cases of very small and very large k.

Configuration:	**Pristine**	**Ortho**	
		L_{30}	**L_{90}**
State	**Transition Energy (eV)**		
1	1.85	1.61	1.84
2	1.88	1.74	1.85
3	1.94	1.84	1.88
4	1.95	1.88	1.94
5	1.95	1.91	1.95
6	1.97	1.98	1.99
7	1.99	1.98	1.99
8	1.99	1.99	2.00
9	2.01	1.99	2.01
10	2.05	2.01	2.04
11	2.05	2.05	2.07
12	2.10	2.07	2.09
13	2.11	2.09	2.10
14	2.13	2.10	2.12
15	2.13	2.12	2.13
Spectroscopic Feature:		E_{11}^{*-}	E_{11}^{*}
Well Depth (eV):		0.36	0.13
Splitting (eV):		0.13	0.01

Table S3. Calculated energies of transition for the experimentally relevant functionalization configurations of (6,5) SWCNTs functionalized with 4-bromobenzene that generate the emission features. Transitions were computed using TDDFT from the optimized ground state geometries. Values highlighted in yellow represent the lowest energy bright state for each species. The well depth is defined as the difference between the energies of the bright transition for the functionalized system vs. that of pristine. The reported splitting is defined as the difference between the energies of the lowest energy bright state and the adjacent higher-energy dark state. Functionalization configurations that generate the deepest wells also exhibit the highest bright-dark state splitting. The ortho-L_{30} configuration is attributed to the E_{11}^{*-} emission features, while the ortho-L_{90} configuration is attributed to E_{11}^{*}.[1]

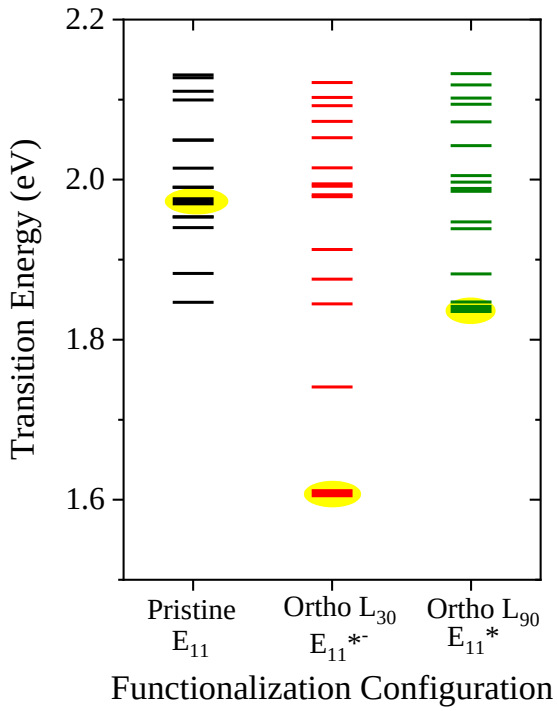

Figure S5. Calculated energies of transition for each experimentally relevant functionalization configuration of (6,5) SWCNTs functionalized with 4-bromobenzene. Transitions were computed using TDDFT from the optimized ground state geometries. The bold states highlighted in yellow represent the lowest-energy bright transition for each functionalization configuration. Those species that generate the deepest wells also exhibit the highest bright-dark state splitting. The ortho-L_{30} configuration is attributed to the E_{11}^{*-} emission features, while the ortho-L_{90} configuration is attributed to E_{11}^{*}.[1]

Low-k limit. In the limit of slow recombination ($k \ll k_0$), the short and long decay times are given by $1/\tau_s = k_0(1+\gamma)$ and $1/\tau_l = k/(1+\gamma)$, where $\gamma = e^{-\epsilon/kT}$ is the Boltzmann factor. The normalized amplitude of the long decay component of the bright state is $\tilde{A}_l = \frac{A_l}{A_s+A_l} = \frac{1}{(1-p_d^0)(1+\gamma)}$. Physically, this corresponds to the following two stages of the exciton relaxation dynamics. First, the exciton population is rapidly equilibrated within the two states with the time constant of τ_s, so that $\frac{p_d}{p_b} = \gamma$. Then, slowly, the exciton recombines via k. If recombination occurred from both the bright and dark state with the same rate constant k, the slow decay time would be $\frac{1}{\tau_l} = k$. However, we assumed that the recombination only happens from the bright exciton state. Since equilibration is rapid, the ratio of population of the bright state to the total exciton population is $1/(1+\gamma)$ at any moment of the slow recombination. Accordingly, the slow decay time is given by $\frac{1}{\tau_l} = \frac{k}{1+\gamma}$.

Immediately upon completion of the first relaxation stage the population of the bright state is $1/(1+\gamma)$, and therefore $A_l = 1/(1+\gamma)$. However, the initial population of the bright state is $1 - p_d^0 = A_s + A_l$. Therefore, the normalized amplitude of the long decay component of the bright state is $\tilde{A}_l = \frac{1}{(1-p_d^0)(1+\gamma)}$.

Large-*k* limit. In the limit of very rapid recombination ($k \gg k_0$), the short and long decay times are given by $\frac{1}{\tau_s} = k + \gamma k_0$ and $\frac{1}{\tau_l} = k_0$. Physically, it means that at the first very rapid stage there occurs an almost complete depletion of the bright state. Since the outflow rate constants for the bright state are k and $k_0' = \gamma k_0$, the resulting effective rate constant of such depletion is $k + \gamma k_0$, and hence τ_s provided above. At the second stage, whatever exciton population is trapped in the dark state relaxes to the bright state with the rate constant k_0, and then almost instantaneously recombines with k. The bottleneck for this two-step second stage is the first slow step, so $\tau_l = 1/k_0$.

The normalized amplitude of the long decay component of the bright state in this limiting case is

$$\tilde{A}_l = \gamma \frac{k_0^2}{k^2} + \frac{k_0(k+k_0-\gamma k_0)}{k^2(1-p_d)} p_d. \tag{16}$$

The first r.h.s. term in this expression is easy to understand if we set p_d to zero. Then, during the rapid depletion stage a small fraction of the bright state population undergoes up-conversion to the dark state. This fraction is $k_0'\tau_s \approx \gamma \frac{k_0}{k}$. This resulting population of the dark state now undergoes relaxation to the bright one, and then almost instantaneously recombines. Since the recombination is assumed rapid, we can apply the quasi-steady-state-approximation for the population of the bright state by setting the inflow and outflow rates for the bright state to be the same. This results in the following relation between the instantaneous populations of the bright and dark states: $p_b = \frac{k_0}{k} p_d$. Since the population of the dark state after the initial rapid stage was $\gamma \frac{k_0}{k}$, the resulting normalized amplitude of the second component is of course $\tilde{A}_l = \gamma \frac{k_0^2}{k^2}$. In the case of non-zero initial population of the dark state, and, therefore, non-unit initial population of the bright state, this expression is corrected by an extra term, resulting in Eq. (16).

Degenerate dark states and recombination from dark states. The model above can be generalized to the case of not a single but $n > 1$ degenerate dark states (still with single bright state though), if the rate constants for up- and down-conversion between *individual* dark and bright states are still k_0' and k_0, respectively. Under these conditions, this new model can be reduced to the previous two-state one, Eq. (14), if the substitution $\gamma \to n\gamma$, and therefore $k_0' \to nk_0'$ is performed, and the down-conversion rate constant k_0 remains intact. One can readily see that the ratio of equilibrium populations is now $\frac{p_d}{p_b} = n\gamma$, that is the detailed balance is satisfied since p_d is now understood as the total population of all n dark states. Therefore, all the expressions for the amplitudes and decay times, derived above for the two-state model, are correct for the single-bright-n-dark-states model if we now treat γ as not just a Boltzmann factor

but $\gamma = ne^{-\epsilon/kT}$ instead. In practice, it means that at sufficiently low dark-bright energy splitting γ can be larger than 1.

Finally, we note that the general solution, Eq. (15), and, therefore, all the above results for limiting cases can be modified exactly if, in addition to all the processes encoded by Eq. (14), we also have an extra recombination channel with identical rate constant k' for the bright and all the dark states (e.g., MPD). This amounts to simple multiplication of $p_d(t)$ and $p_b(t)$ in Eq. (15) by $e^{-k't}$. Therefore, the inclusion of such an extra channel change shortens the decay times, but leaves the component amplitudes intact.

III. Synthesis of S-PBn(b)-Ph4 Polymer

Instrumentation. Free, unbound polymer in each polymer/SWNT sample was removed using a GE/ÄKTApurifier HPLC system (GE Healthcare Bio-Science AB, Björkgatan, Uppsala, Sweden) equipped with two preparative columns (160x16 mm each; stationary phase: sephacryl S-500 and S-200) connected in a series. The HPLC system uses three-wavelength detection, which distinguishes fractions that contain SWNTs. Electronic spectra were recorded on a Varian 5000. NMR spectra were recorded on either a 400 or 500 MHz AC-Bruker spectrometer. Chemical shifts for ^{1}H NMR spectra are relative to residual protium in deuterated solvent ($CDCl_3$ = 7.26 ppm, D_2O = 4.75 ppm). All *J* values are reported in Hertz. MALDI-TOF mass spectroscopic data were obtained with a Perspective Voyager DE instrument (Department of Chemistry, Duke University). Microwave-assisted reactions were performed using an Emrys Personal Chemistry System (Biotage).

6,6'-dibromo-[1,1'-binaphthalene]-2,2'-diol (S-1, see Scheme 1): To a two neck round bottom flask fitted with addition funnel, [1,1'-binaphthalene]-2,2'-diol (15.0 g, 52.4 mmol) was added, dissolved in methylene chloride (~400 mL) and cooled to -78°C. Bromine (7.3mL, 141.5 mmol) was diluted in methylene chloride (100 mL) and added to the addition funnel. The bromine mixture was added dropwise. The reaction was allowed to warm to room temperature and stirred overnight. Reaction was cooled to 0°C and quenched with Na_2SO_3. The mixture was allowed to stir for 1h. The organic layer was separated and washed with brine (3 x 200 mL) dried over Na_2SO_4 and concentrated in vacuo. No further purification was needed. Product was obtained as an off white crystalline powder (24.5 g, 50% yield): ^{1}H NMR (400 MHz, $CDCl_3$) δ 8.04 (d, J = 2.0 Hz, 2H), 7.88 (d, J = 8.9 Hz, 2H), 7.40 – 7.34 (m, 4H), 6.95 (d, J = 9.0 Hz, 2H), 5.02 (s, 2H). MS (MALDI-TOF) m/z: 442.73 [($M+H^+$), calcd 443.00].

15,20-dibromo-7-(2-(2-(2-methoxyethoxy)ethoxy)ethoxy)-4H,10H-5,9-(metheno)dinaphtho[2,1-b:1',2'-d][1,6]dioxacyclotridecine (S-2): To a round bottom flask was added S-1 (5.46 g, 12.75 mmol) dissolved in degassed dimethylformamide (300 mL). The mixture was heated to 80°C. 1,3-bis(bromomethyl)-5-(2-(2-(2-methoxyethoxy)ethoxy)ethoxy)benzene was taken up in degassed dimethylformamide (50 mL) and added to the prepared mixture over 16h using a syringe pump. After an additional 8h, saturated brine (300 mL) was added, then extracted with EtOAc (3 x 200 mL). The combined organic layers were dried over Na_2SO_4 and concentrated in vacuo. The crude product was purified by column chromatography on silica gel (CH_2Cl_2/MeOH : 95/5) to afford product as a

yellow crystalline solid (4.22 g , 58% yield): ^{1}H NMR (400 MHz, $CDCl_3$) δ 7.95 (d, 2H, J = 2.4 Hz), 7.782 (d, 2H, J = 8.8 Hz), 7.408 (d, 2H, J = 8.8 Hz), 7.331 (d, 2H, J = 2.0 Hz), 7.308 (d, 2H, J = 2.0 Hz), 7.059 (d, 2H, J = 8.8 Hz), 6.977 (broad s, 1H), 6.453 (d, 2H, J = 1.2 Hz), 5.169 (d, 2H, J = 12.4 Hz), 4.997 (d, 2H, J = 12.4 Hz), 4.001-3.887 (m, 2H, J = 4.4 Hz), 3.737 (t, 2H, J = 4.4 Hz), 3.660-3.619 (m, 6H, 3.550-3.257 (m, 2H), 3.30 (s, 3H)). MS (MALDI-TOF) m/z: 706.53 [(M+H$^+$), calcd 707.14].

((20-ethynyl-7-(2-(2-(2-methoxyethoxy)ethoxy)ethoxy)-4H,10H-5,9-(metheno)dinaphtho[2,1-b:1',2'-d][1,6]dioxacyclotridecin-15-yl)ethynyl)triisopropylsilane (S-3): To a round bottom flask was added S-2 (5.0 g, 7.1 mmol), tetrakis(triphenylphosphine)palladium(0) (1.6 g, 1.4 mmol), and copper(I) iodide (138 mg, 0.7 mmol). A solution of THF (150 mL), diisopropylamine (50 mL), and (triisopropylsilyl)acetylene (9.5 mL, 42.6 mmol) was degassed using a freeze, pump, thaw (3x) technique and then cannulated into the flask. The reaction was heated to 60°C and stirred for 20h. After cooling to room temperature, saturated brine (200 mL) was added and extracted with EtOAc (3 x 200 mL). The combined organic layers were dried over over Na_2SO_4 and concentrated in vacuo. The crude product was purified by column chromatography on silica gel (EtOAc/CH_2Cl_2/hexane : 4/3/3) to afford product as a yellow-brown crystalline solid (4.6 g , 72% yield): ^{1}H NMR (400 MHz, $CDCl_3$) δ 7.951 (d, 2H, J = 1.6 Hz), 7.815 (d, 2H, J = 9.2 Hz), 7.388 (d, J = 8.8 Hz), 7.302 (dd, 2H, J = 8.8 Hz, 1.6 Hz), 7.134 (d, 2H, J = 8.8 Hz), 6.964 (br s, 1H), 6.438 (s, 2H), 5.166 (d, 2H, J = 12.4 Hz), 4.977 (d, 2H, J = 12.4 Hz), 3.997-3.902 (m, 2H), 3.737 (t, 2H, J = 4.4 Hz), 3.661- 3.585 (m, 6H), 3.547-3.524 (m, 2H), 3.32 (s, 3H), 1.168-1.068 (m, 42H)). MS (MALDI-TOF) m/z: 912.94 [(M+H$^+$), calcd 911.58].

15,20-diethynyl-7-(2-(2-(2-methoxyethoxy)ethoxy)ethoxy)-4H,10H-5,9-(metheno)dinaphtho[2,1-b:1',2'-d][1,6]dioxacyclotridecine (S-4): To a round bottom flask was added S-3 (1.5 g, 1.6 mmol) dissolved in THF (100 mL). The solution was cooled to 0°C. A solution of tetra-n-butylammonium fluoride (3.5 mL, 3.5 mmol) was added dropwise. The mixture was stirred for 10m, warmed to room temperature and stirred an additional 5m. A mixture of methanol (10 mL) and water (0.1 mL) was added to quench the reaction. Mixture was dried in vacuo and purified by column chromatography on silica gel (CH_2Cl_2/MeOH : 95/5) to afford product as a yellow-brown oil that was immediately used in the next reaction (958 mg , ~99% yield).

((((7-(2-(2-(2-methoxyethoxy)ethoxy)ethoxy)-4H,11H-5,9-(metheno)dinaphtho[2,1-b:1',2'-d][1,7]dioxacyclotridecine-15,20-diyl)bis(ethyne-2,1-diyl))bis(2,5-bis(2-(2-(2-methoxyethoxy)ethoxy)ethoxy)-4,1-phenylene))bis(ethyne-2,1-diyl))bis(triisopropylsilane) (S-5): To a round bottom flask was added S-4 (160 mg, 0.27 mmol), ((4-iodo-2,5-bis(2-(2-(2-methoxyethoxy)ethoxy)ethoxy)phenyl)ethynyl)triisopropylsilane (565 mg, 0.8 mmol), tetrakis(triphenylphosphine)palladium(0) (70 mg, 0.06 mmol), and copper(I) iodide (10 mg, 0.03 mmol). A solution of THF (100 mL) and diisopropylamine (25 mL) was degassed using a freeze, pump, thaw (3x) technique and cannulated into the reaction flask. Mixture was heated to 60°C for 20h then allowed to cool to room temperature. The mixture was filtered through a plug of celite and concentrated in vacuo. Crude product was purified by column chromatography on silica gel (CH_2Cl_2/MeOH : 95/5) to afford product as a brown solid (440 mg , ~99% yield): ^{1}H NMR (400 MHz, $CDCl_3$) δ 7.98 (s, 2H), 7.84 (d, 2H), 7.41 (d, 2H), 7.33 (d, 2H), 7.17 (d, 2H),

7.04 (s, 1H), 7.01 (s, 2H), 6.98 (s, 2H), 6.45 (s, 2H), 5.19 (d, 2H), 5.00 (d, 2H), 4.16 (m, 10H), 3.87 (m, 10H), 3.77 (m, 10H), 3.50-3.67 (m, 30H), 3.34 (s, 9H), 3.28 (s, 6H), 1.03 (36H)). MS (MALDI-TOF) m/z: 1757.86 [($M+H^+$), calcd 1759.00].

15,20-bis((4-ethynyl-2,5-bis(2-(2-(2-methoxyethoxy)ethoxy)ethoxy)phenyl)ethynyl)-7-(2-(2-(2-methoxyethoxy)ethoxy)ethoxy)-4H,11H-5,9-(metheno)dinaphtho[2,1-b:1',2'-d][1,7]dioxacyclotridecine (S-6): To a round bottom flask was S-5 (225 mg, 0.14 mmol) dissolved in THF (100 mL). The solution was cooled to 0°C. A solution of tetra-n-butylammonium fluoride (0.3 mL, 0.31 mmol) was added dropwise. The mixture was stirred for 10m, warmed to room temperature and stirred an additional 5m. A mixture of methanol (10 mL) and water (0.1 mL) was added to quench the reaction. Mixture was dried in vacuo and purified by column chromatography on silica gel (CH_2Cl_2/MeOH : 95/10) to afford product as a yellow-brown oily solid that was immediately used in the next reaction (174 mg , ~99% yield).

Polymer S-PBn(b)-Ph4 (S-7): To a microwave vial was added S-6 (174 mg, 0.14 mmol), 3,3',3",3'"-(4,4'-dibromo-[1,1'-biphenyl]-2,2',5,5'-tetrayl)tetrakis(propane-1-sulfonate) (101 mg, 0.13 mmol), tetrakis(triphenylphosphine)palladium(0) (29 mg, 0.025 mmol), and copper(I) iodide (3 mg, 0.013 mmol). The vial was purged and back filled with Argon (3 x 30 min). A solution of DMF (9 mL), water (6 mL), and diisopropylamine (3 mL) was degassed by gently bubbling argon through the solution while stirring for 3h. Solvent mixture was cannulated into vial and heated by microwave to 160°C for 1h. Mixture was then heated by oil bath at 70°C for 20h. The mixture was heated an additional 2h after the addition of polymer cap (100 mg) dissolved in degassed DMSO (10 mL). The mixture was allowed to cool to room temperature and basified with a solution of NaCl / K_2CO_3 (1/1). The mixture was added to a solution of Acetone / Et_2O / MeOH (5/4/1). The resulting precipitate was collected by filtration and washed with Acetone / Et_2O / MeOH solution (5/4/1). The precipitate was purified using size exclusion chromatography. The purified product (9 mg, ~3% yield) was taken up in a water / MeOH mixture (7/3 : 6 mL).

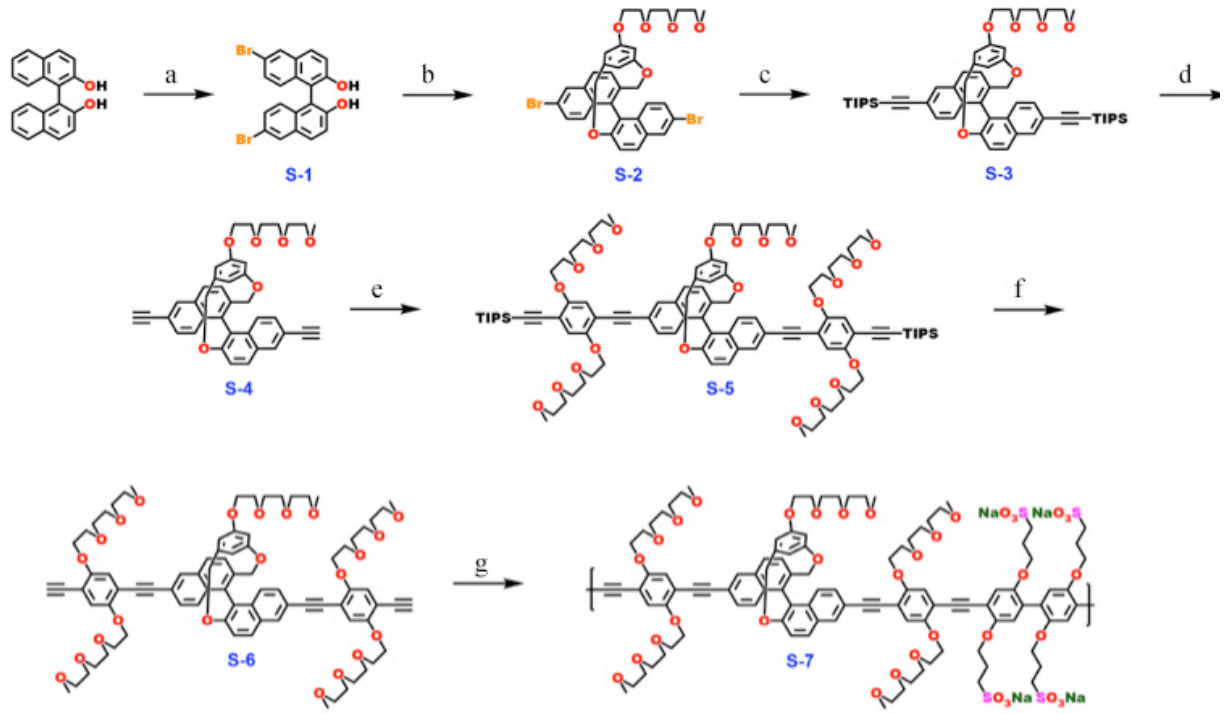

Scheme 1. Synthetic route to S-PBN(b)-Ph_4 polymer. a) Br_2 in DCM, -78°C to rt, 24h. b) S-4, K_2CO_3 in DMF, 80°C, 24h. c) TIPS acetylene, $Pd(PPh_3)_4$, CuI, TEA, in THF, 60°C, 24h. d) TBAF in THF, 0°C to rt, 15m. e) ((4-iodo-2,5-bis(2-(2-(2-methoxyethoxy)ethoxy)ethoxy)phenyl)ethynyl)triisopropylsilane, $Pd(PPh_3)_4$, CuI, TEA, in THF, 60°C, 24h. f) TBAF in THF, 0°C to rt, 15m. g) 3,3',3",3'"-(4,4'-dibromo-[1,1'-biphenyl]-2,2',5,5'-tetrayl)tetrakis(propane-1-sulfonate), $Pd(PPh_3)_4$, CuI, DIPA, in DMF/H_2O, 70°C, 24h.

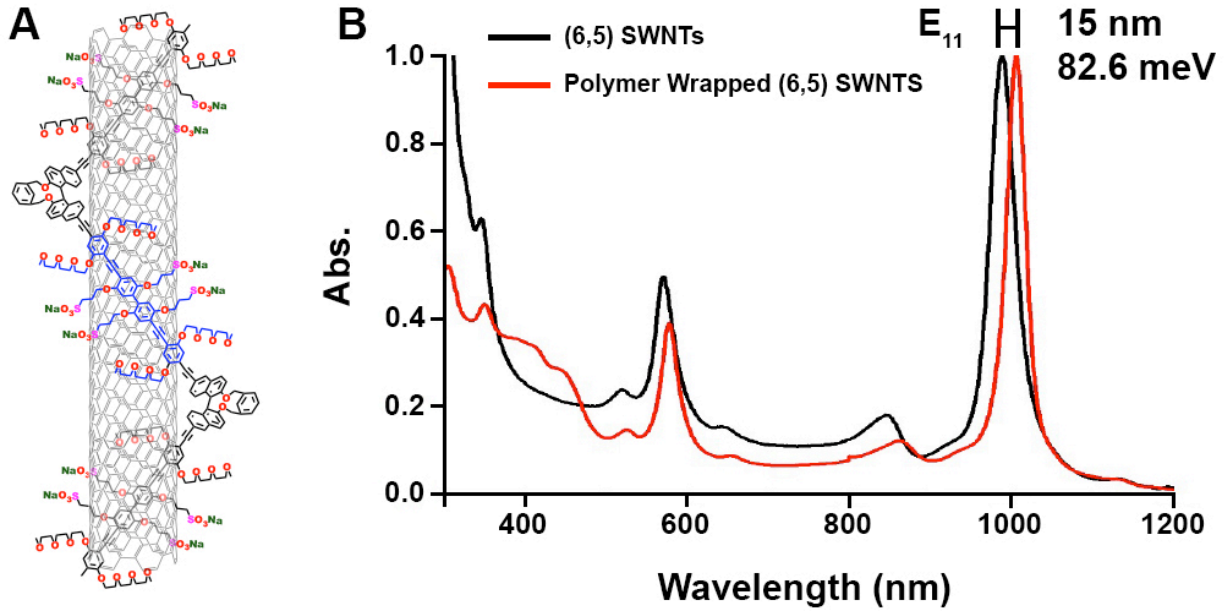

Figure S6. A) Graphical representation of polymer wrapped [6,5] SWCNT B) UV-vis spectrum of surfactant encapsulated [6,5]SWNT sample and S-PBN(b)-Ph_4 wrapped [6,5] SWCNT sample. A 15 nm bathochromic shift is observed after polymer wrapping.

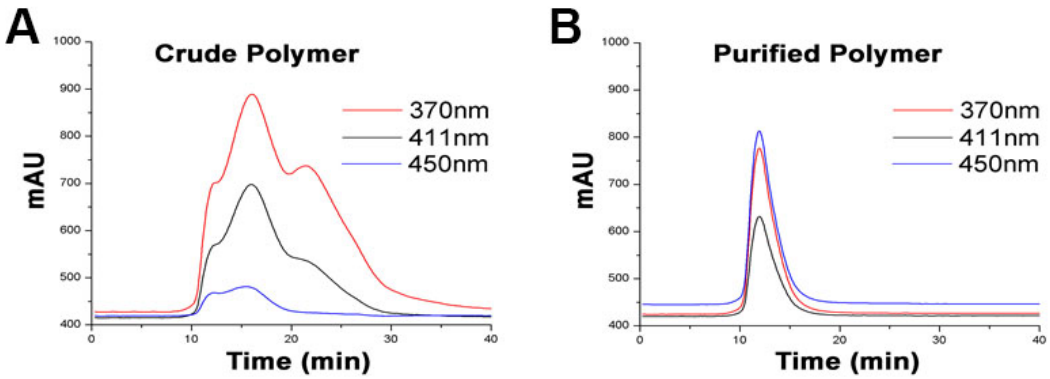

Figure S7. A) GPC trace of crude polymer S-PBN(b)-PH_4 with targeted length fractions highlighted B) GPC trace of ~10 mer purified S-PBN(b)-Ph_4

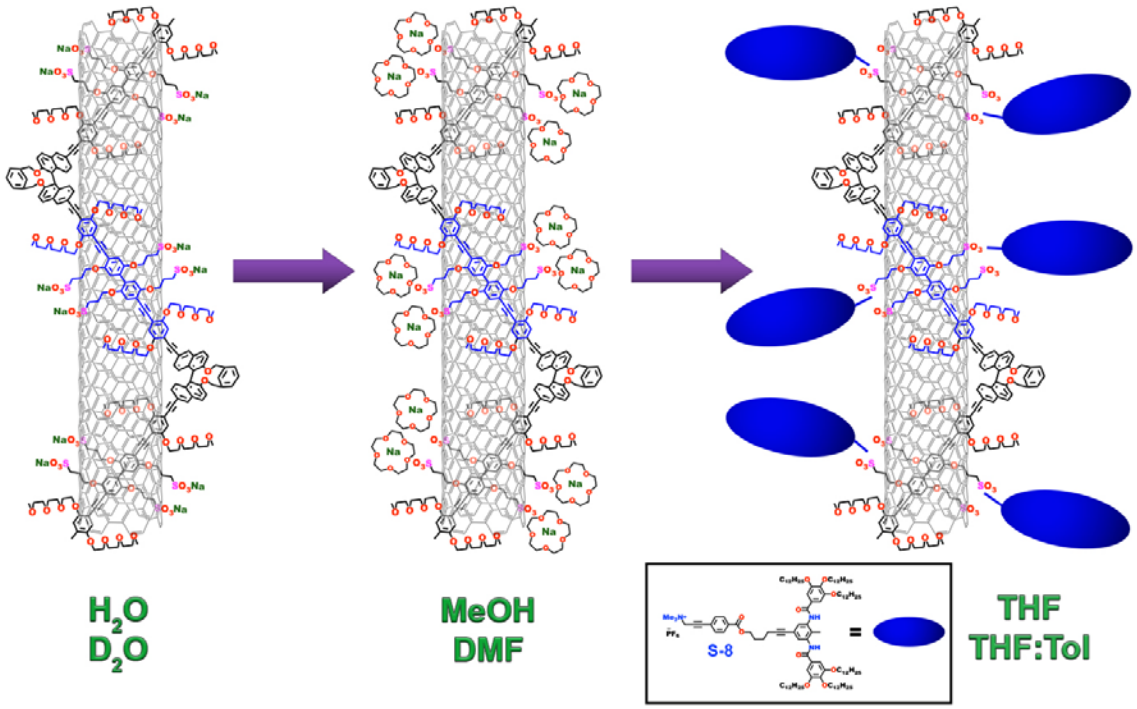

Figure S8. Depiction of polymer wrapped doped [6,5] SWCNT samples being dispersed in various solvents, mediated by solubilizing counterions.[15]

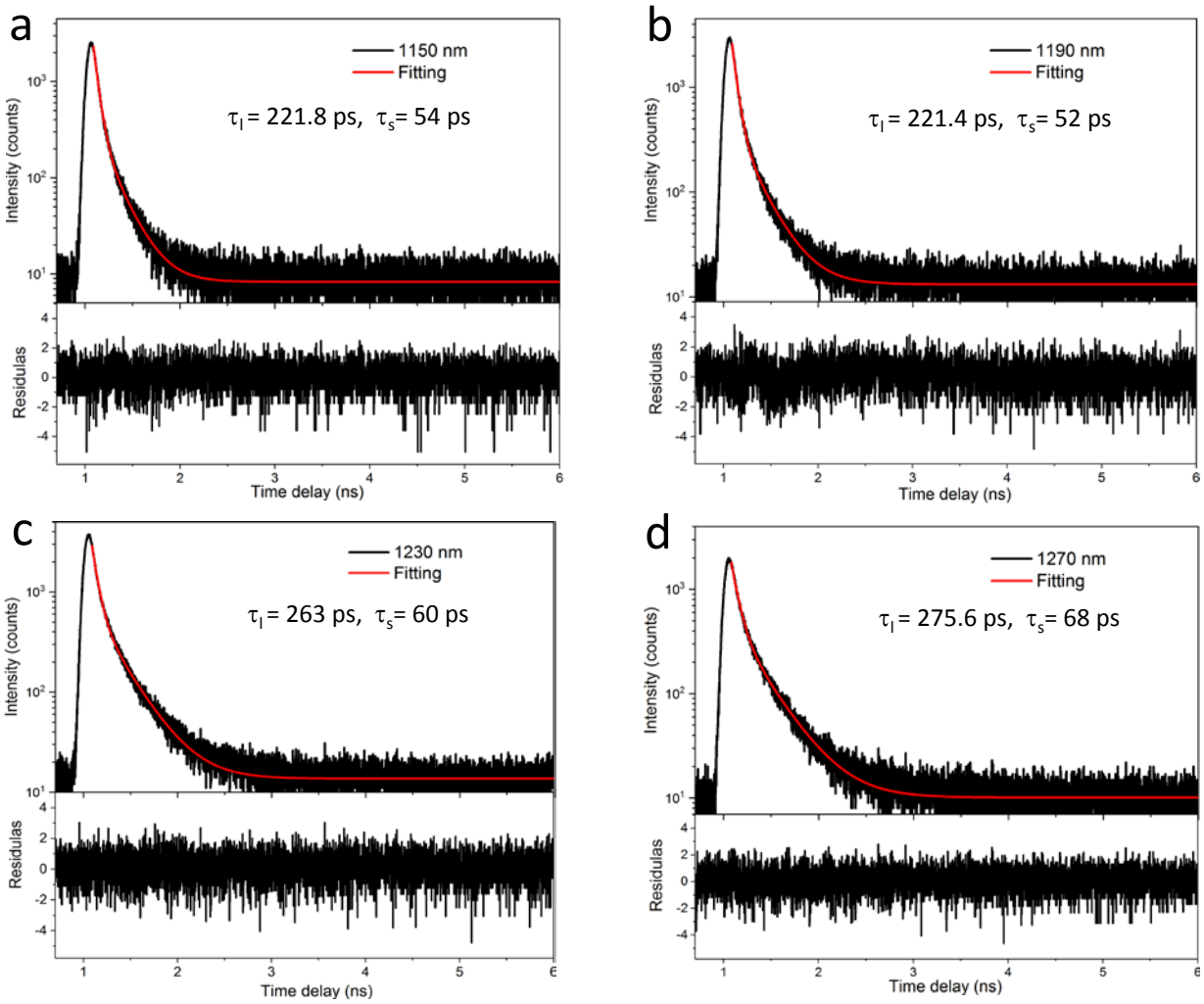

Figure S9. Example PL intensity decay curves for 4-methoxybenzene-functionalized (6,5) SWCNTs suspended in 20% THF/80% Toluene, obtained at 4 different excitation wavelengths: a) 1150 nm, b) 1190 nm, c) 1230 nm, and d) 1270 nm. Experimental data in black and reconvolution fitting result in red. Lower panel for each curve displays the respective fitting residuals.

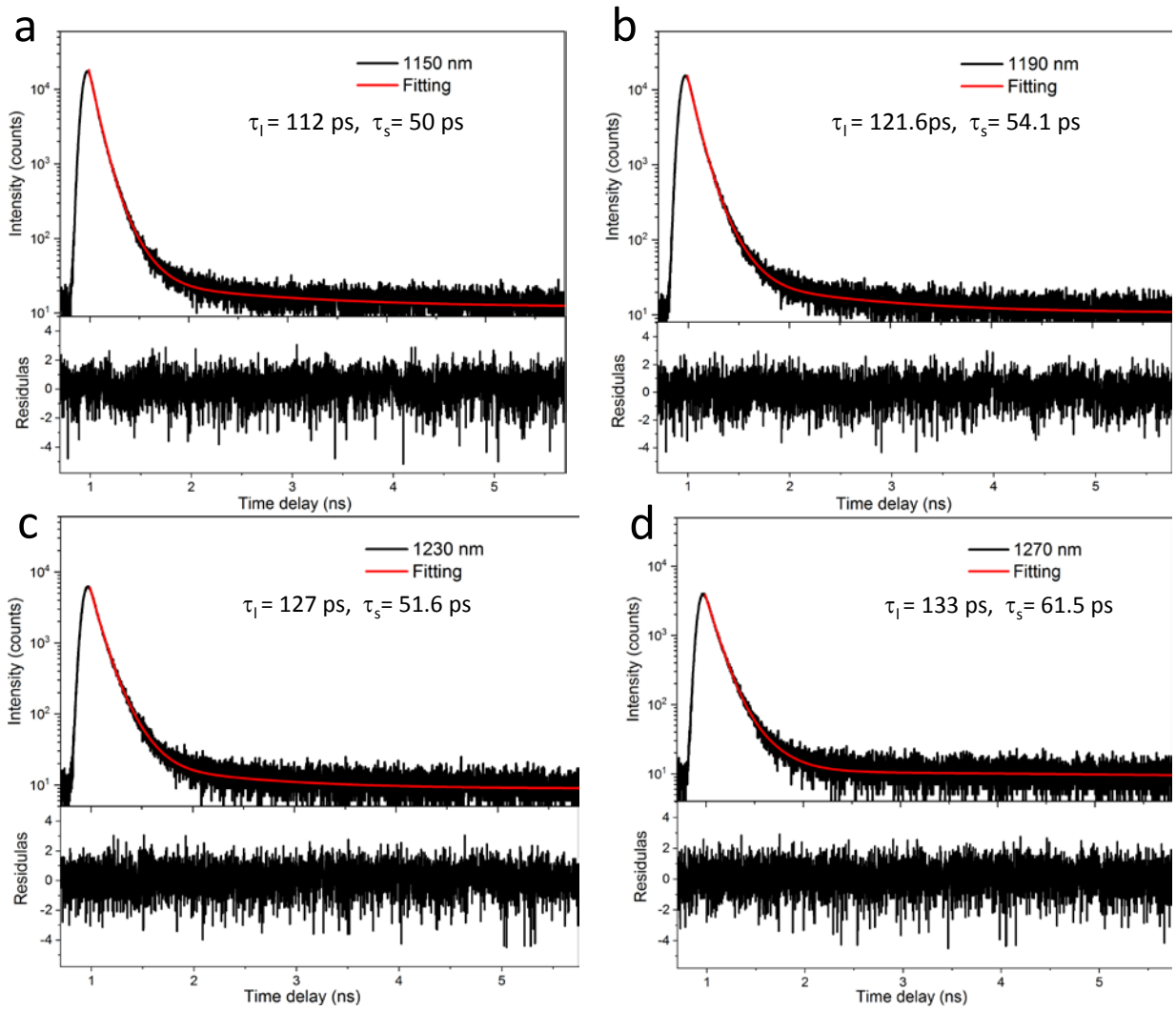

Figure S10. Example PL intensity decay curves for 4-methoxybenzene-functionalized (6,5) SWCNTs suspended in H_2O, obtained at 4 different excitation wavelengths: a) 1150 nm, b) 1190 nm, c) 1230 nm, and d) 1270 nm. Experimental data in black and reconvolution fitting result in red. Lower panel for each curve displays the respective fitting residuals.

References

1. He, X.; Gifford, B. J.; Hartmann, N. F.; Ihly, R.; Ma, X.; Kilina, S. V.; Luo, Y.; Shayan, K.; Strauf, S.; Blackburn, J. L.; Tretiak, S.; Doorn, S. K.; Htoon, H. Low-Temperature Single Carbon Nanotube Spectroscopy of sp3 Quantum Defects. *ACS Nano* **2017**, *11*, 10785−10796.

2. Miyauchi, Y.; Iwamura, M.; Mouri, S.; Kawazoe, T.; Ohtsu, M.; Matsuda, K. Brightening of Excitons in Carbon Nanotubes on Dimensionality Modification. *Nat. Photon.* **2013**, *7*, 715-719.

3. Kim, M.; Adamska, L.; Hartmann, N. F.; Kwon, H.; Liu, J.; Velizhanin, K. A.; Piao, Y.; Powell, L. R.; Meny, B.; Doorn, S. K.; Tretiak, S.; Wang, Y. Fluorescent Carbon Nanotube Defects Manifest Substantial Vibrational Reorganization. *J. Phys. Chem. C* **2016**, *120*, 11268-11276.

4. Perebeinos, V., Tersoff, J.; Avouris, P. Radiative Lifetime of Excitons in Carbon Nanotubes. *Nano Lett.* **2005**, *5*, 2495-2499.

5. Berestetskii, V. B.; Lifshitz, E. M.; Pitaevskii, L. P. *Quantum Electrodynamics*. 2 ed. Vol. 4. 1982, London: Pergamon.

6. Gaponenko, S. V. *Introduction to Nanophotonics*. 2010, Cambridge, UK: Cambridge University Press.

7. Jackson, J. D. *Classical Electrodynamics*. 3 ed. 1998, New York: Wiley.

8. Perebeinos, V.; Tersoff, J.; Avouris, P. Scaling of Excitons in Carbon Nanotubes. *Phys. Rev. Lett.* **2004**, *92*, 257402.

9. Novotny, L.; Hecht,B. *Principles of Nano-Optics*. 1 ed. 2006, Cambridge, UK: Cambridge University Press.

10. Klots, A. R.; Weintrub, B.; Prasai, D.; Kidd, D.; Varga, K.; Velizhanin, K. A.; Bolotin, K. L. Controlled Dynamic Screening of Excitonic Complexes in 2D Semiconductors. *Sci. Rep.* **2018**, *8*, 768.

11. Wen, Q.; Kershaw, S. V.; Kalytchuk, S.; Zhovtiuk, O.; Reckmeier, C.; Vasilevskiy, M. I.; Rogach, A. L. Impact of D2O/H2O Solvent Exchange on the Emission of HgTe and CdTe Quantum Dots: Polaron and Energy Transfer Effects. *ACS Nano* **2016**, *10*, 4301-4311.

12. Klimov, V. I. *Nanocrystal Quantum Dots*. 2 ed. 2010, Boca Raton, FL, USA: CRC Press.

13. Homma, Y.; Chiashi, S.; Yamamoto, T.; Kono, K.; Matsumoto, D.; Shitaba, J.; Sato, S. Photoluminescence Measurements and Molecular Dynamics Simulations of Water Adsorption on the Hydrophobic Surface of a Carbon Nanotube in Water Vapor. *Phys. Rev. Lett.* **2013**, *110*, 157402.

14. Vijayaraghavan, V.; Wong, C. H. Torsional Characteristic of Single Walled Carbon Nanotube with Water Interactions by Using Molecular Dynamics Simulations. *Nano-Micro Lett.* **2014**, *6*, 268-279.

15. Olivier, J. H.; Deria, P.; Park, J.; Kumbhar, A.; Andrian-Albescu, M.; Therien, M. J. Ionic Self-Assembly Provides Dense Arrays of Individualized, Aligned Single-Walled Carbon Nanotubes. *Ang. Chem*. **2013**, *52*, 13080-13085.